Influence of Microcracking on Shear Localization

D. H. Warner, M.ASCE[1]; and S. N. Mathaudhu[2]

Abstract: This work examines the influence of microcracking on a material's tendency to shear localize under compressive loading. A two-dimensional (2D) finite-element framework with explicit crack representation using cohesive-element methodologies is employed. The influence of microcracking is examined by taking the fracture toughness of the cohesive elements as a free parameter. The simulations suggest that an optimum fracture toughness exists for promoting shear localization. This value corresponds to the limiting mode I fracture toughness, below which microscopic material defects lead to brittle compressive failure, as opposed to shear localization. While in the presence of confinement, this value is shown to be close to zero; in the absence of confinement, it is computed to be 28% of the shear band toughness for the specific case of ultrafine-grained tungsten. More generally, it is found that the ratio of mode I fracture toughness to shear band toughness provides a crude indicator for predicting whether material defects are likely to lead to brittle failure or enhanced shear localization.
DOI: 10.1061/(ASCE)EM.1943-7889.0000269.

CE Database subject headings: Cracking; Localization; Micromechanics; Finite element method.

Author keywords: Microcracking; Shear banding; Shear localization; Micromechanics; Finite-element modeling.

Introduction

Both the mechanics and materials research communities have long been interested in predicting the conditions that trigger a material to transition from deforming homogeneously to deforming in a localized manner. Technologically, this transition in deformation behavior is most commonly viewed as a negative occurrence that foreshadows a material's loss in its load-bearing capacity. However, in ballistic applications, a transition to localized deformation can be a desired phenomenon. The localization of deformation in a kinetic energy penetrator inhibits the formation of a blunted nose as the penetrator plows through the target. The narrower profile associated with a nonblunting nose equates to a greater penetration depth per amount of material displaced, yielding a more effective penetrator (Magness 1994).

Criteria for the onset of strain localization have existed since the late 1800s, beginning with Considere's criterion for strain localization of a tensile bar (Considere 1885): $\sigma = \partial\sigma/\partial\epsilon$, with σ and ϵ being the true stress and true strain, respectively. For the case of compression, a material's propensity to shear localize can be quantified by a parameter α, which is a function of its strain-hardening rate and strain-rate sensitivity (Jonas et al. 1976). The larger the value of α, the higher the propensity for shear localization or shear banding:

$$\alpha = (\gamma - 1)/m \tag{1}$$

The first term, γ, represents the normalized strain-hardening rate and is expressed as

$$\gamma = \frac{1}{\sigma}\frac{\partial\sigma}{\partial\epsilon}\bigg|_{\dot{\epsilon}} \tag{2}$$

with σ = uniaxial flow stress; ϵ = the uniaxial strain; and $\dot{\epsilon}$ = the strain rate. The second term, m, represents the strain-rate sensitivity of the flow stress and is defined as

$$m = \frac{\partial \ln\sigma}{\partial \ln\dot{\epsilon}} \tag{3}$$

From Eq. (1), it is clear that materials that have a high strain-rate sensitivity and high strain hardening will have a low susceptibility to shear localization. More recently, Wright has defined a shear band susceptibility parameter that includes a material's thermal softening behavior (Wright 2002).

A material property that has not been quantified with respect to its role in shear localization is fracture toughness or susceptibility to microcracking. This property is of particular interest to kinetic energy penetrator applications where materials with low fracture toughness, such as polycrystalline tungsten, are of interest. In the case of polycrystalline tungsten, the low fracture toughness can be considered a somewhat controllable parameter as it is partly governed by the segregation of impurities to the grain boundaries (Briant and Banerji 1983; Lassner and Schubert 1998). Therefore, by altering impurity content during processing, the fracture toughness and microcracking can be controlled (Stephens 1963). However, it is unclear how microcracking influences shear localization, and, thus, the amount of processing effort that should be devoted to control this property is unclear. Experimentally, postmortem micrographs often show microcracking in tungsten samples that deformed homogeneously, whereas little microcracking is observed in samples that shear localize (Wei et al. 2006b). Nonetheless, from these observations alone one cannot conclude that microcracking inhibits shear localization, as the samples differ by more than fracture toughness.

This work attempts to directly examine the role of microcracking and fracture toughness on a material's tendency to undergo shear localization. It utilizes a two-dimensional (2D) finite-element framework with cohesive element methodology. A substantial component involves the challenge of explicitly modeling multiple

[1]Assistant Professor, School of Civil and Environmental Engineering, Cornell Univ., Ithaca, NY 14853 (corresponding author). E-mail: address: dhw52@cornell.edu

[2]Scientist, U.S. Army Research Laboratory, Aberdeen Proving Ground, MD 21005.

Note. This manuscript was submitted on June 8, 2010; approved on April 4, 2011; published online on April 5, 2011. Discussion period open until March 1, 2012; separate discussions must be submitted for individual papers. This paper is part of the ***Journal of Engineering Mechanics***, Vol. 137, No. 10, October 1, 2011. ©ASCE, ISSN 0733-9399/2011/10-691–698/$25.00.

interacting cracks in compression. For this, a recently developed multibody interface/contact algorithm is utilized (Warner and Molinari 2006). The 2D model problem is fashioned after an ultrafine-grained tungsten plate transected with weak potential fracture paths, e.g., embrittled grain boundaries. The fracture toughness of these paths is taken as a free parameter, and for simplicity is assumed uniform within each simulation. Simulations are performed with cohesive element fracture toughnesses ranging from zero to 15 MPa$\sqrt{m}$. This range of values gives behavior that spans brittle fracture to ductile flow. Motivated both by scientific inquiry and kinetic energy (KE) penetrator application, the effects of confining pressure and strain rate are also examined. The mechanism ultimately controlling the brittle versus ductile behavior are identified, and an additional set of more focused simulations is carried out. Through these studies, an upper bound of the mode I fracture toughness needed to suppress brittle failure is estimated. When the mode I fracture toughness is higher than this value, microscopic material defects are forecasted to enhance a materials tendency to shear localize.

Methodology

Finite-Element Framework

The finite-element analysis was performed within a total Lagrangian framework using an explicit dynamic methodology (Belytschko et al. 2000). A standard six node isoparametric triangular element was used to discretize the 2D specimen domain. Field quantities were integrated using three Gauss points (Hughes 1987). By choosing an explicit time integration routine, the transmission of contact forces across crack faces can be easily addressed by dividing the time integration procedure into two distinct parts. First, the kinematic variables were incrementally updated without regard for the contact constraints. Using these nodal positions, contact is then enforced.

The discrete equations of motion for each node at time $t^{n+1} = t^n + \Delta t$ were determined using a modified central difference scheme where Δt was chosen to be $0.1h/\sqrt{C_{11}/\rho}$, a value sufficiently less than the numerical stability limit (Bathe and Wilson 1976), where ρ and h correspond to the density and minimum element size, respectively. The unconstrained displacement vector $\hat{\mathbf{u}}_i^{n+1}$, acceleration $\hat{\mathbf{a}}_i^{n+1}$, and velocity $\hat{\mathbf{v}}_i^{n+1}$ of node i was updated as

$$\hat{\mathbf{a}}_i^n = \frac{\mathbf{f}_i^n}{m_i} \tag{4}$$

$$\hat{\mathbf{v}}_i^{n+1} = \mathbf{v}_i^n + \hat{\mathbf{a}}_i^n \Delta t \tag{5}$$

$$\hat{\mathbf{u}}_i^{n+1} = \mathbf{u}_i^n + \hat{\mathbf{v}}_i^{n+1} \Delta t \tag{6}$$

with m_i = lumped mass of node i; and $\mathbf{f}_i^n$ = residual force vector, which was calculated at the element level.

The corrected displacements vectors $\mathbf{u}_i^{n+1}$, accelerations $\mathbf{a}_i^n$, and velocities $\mathbf{v}_i^{n+1}$ were computed from a corrective force calculated from the unconstrained displacements $\hat{\mathbf{u}}_i^{n+1}$ in a manner similar to Eqs. (4)–(6). In the case of interpenetration of a node i into a surface defined by nodes j and k, the correction force, $\mathbf{f}_i^{\text{corr}}$, was calculated as

$$\mathbf{f}_i^{\text{corr}} = \frac{\boldsymbol{\delta}_i}{2\Delta t^2 (1/m_i + 1/m_i^s)} \tag{7}$$

where

$$m_i^s = \alpha m_j + (1-\alpha) m_k \tag{8}$$

with α = weighting factor between 0 and 1 specifying the relative proximity of node i to nodes j and k on the contact surface; and $\boldsymbol{\delta}_i$ = shortest vector between node i and the contact surface. [In some special cases, $\boldsymbol{\delta}_i$ is not the shortest vector between node i and the contact surface. See Taylor and Flanagan (1987) for more details.] To preserve linear momentum, an opposing force was applied to the contact surface through nodes j and k as

$$\mathbf{f}_j^{\text{corr}} = -\alpha \mathbf{f}_i^{\text{corr}} \tag{9}$$

$$\mathbf{f}_k^{\text{corr}} = -(1-\alpha) \mathbf{f}_i^{\text{corr}} \tag{10}$$

The factor of $1/2$ in Eq. (7) is attributable to i representing a loop over all nodes (mixed master-slave algorithm).

Alternatively, in the case of adhesion, the sign of $\boldsymbol{\delta}_i$ was opposite that of interpenetration. Thus, $\mathbf{f}_i^{\text{corr}}$ acted as a tensile force across the interface. In adhesion, the value of $\mathbf{f}_i^{\text{corr}}$ from Eq. (7) is never permitted to exceed half of the force given by the cohesive law. The calculation of frictional forces was identical to the computation of those for adhesion except that $\boldsymbol{\delta}_i$ in Eq. (7) was a vector acting to erase the unconstrained relative tangential displacement increment of the current time step.

Finally, to account for the interaction of a single node with multiple bodies, as is the case when three potential crack paths intersect, two passes of the correctional phase of the algorithm were conducted. In the second pass, only those interactions not identified on the first were considered.

Constitutive Laws

An associative isotropic elastic-plastic von Mises constitutive law was used to describe the response of ultrafine-grained tungsten (Wei et al. 2006a). The yield surface was represented by

$$\sigma_y = \sigma_{y_0} \left(1 + \frac{\epsilon_{\text{eps}}^n}{\epsilon_{\text{eps}_0}} + \frac{\dot{\epsilon}_{\text{eps}}^m}{\dot{\epsilon}_{\text{eps}_0}}\right) \left[1 - \left(\frac{T - T_{\text{room}}}{T_{\text{melt}} - T_{\text{room}}}\right)^{\alpha}\right] \tag{11}$$

where ϵ_{eps}, $\dot{\epsilon}_{\text{eps}}$, and T evolve during the simulation and represent the equivalent plastic strain, equivalent plastic strain rate, and temperature, respectively; σ_{y_0}, ϵ_{eps_0}, and $\dot{\epsilon}_{\text{eps}_0}$ serve as fitting parameters and are often referred to as a reference flow stress, reference strain, and reference strain rate. These values were chosen as 590 MPa, 0.01, and 0.1 s^{-1}, respectively. The exponents n, m, and α control the rate of strain hardening, strain-rate sensitivity, and thermal softening, and were chosen as 0.04, 0.055, and 0.4055, respectively. The thermal softening was fit to the experimental data of Lennon and Ramesh (2000). T_{melt} was taken as 3,683 K and T_{room} as 293 K. Adiabatic conditions were assumed, and the specific heat was taken as 134 J/kgK. Ninety percent of the plastic work was assumed to be converted into heat. A shear modulus of 161 GPa and Young's modulus of 411 GPa governed the elastic response, and the density was taken as 19,250 kg/m^3. The finite deformation plasticity framework follows Cuitino and Ortiz (1992) and is based on a multiplicative decomposition of the deformation gradient.

For both tension and shear, the separation of fracture interfaces was controlled by a cohesive law (Barenblatt 1962; Dugdale 1960). The normal, δ_n, and shear δ_s opening displacements at an interface were combined to give an effective measure of separation following the relation

$$\delta_{\text{eff}} = \sqrt{\delta_n^2 + \beta \delta_s^2} \tag{12}$$

where β = empirical parameter used to assign a weighting to shear versus normal opening. In this study, a value of 0.7 was used,

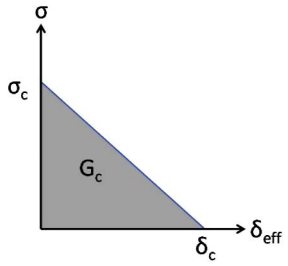

Fig. 1. Initially rigid, linearly decreasing cohesive law used in this work

giving a mode II fracture toughness of 1.09 times the mode I fracture toughness.

A reversible linear decreasing cohesive law was used to model interface stress, as shown in Fig. 1. When the traction on the interface becomes greater than σ_c, the interface begins to open and δ_{eff} obtains nonzero values. At $\delta_{\text{eff}} = \delta_c$, the interface traction attributable to the cohesive law goes to zero for the remainder of the simulation. This gives a mode I fracture energy release rate of

$$G_c = \frac{1}{2}\sigma_c \delta_c \tag{13}$$

Just prior to crack propagation, the cohesive zone will extend a length of (Palmer and Rice 1973)

$$l_z = \frac{9\pi}{32}\frac{E}{1-\nu}\frac{G_c}{\sigma_c^2} \tag{14}$$

If the neighboring bulk elements are linear elastic in nature, then G_c is typically chosen to match the material properties, and σ_c is chosen such that l_z is resolved by the mesh. The value of δ_c is then specified by Eq. (13). In the cases investigated in this study, where the bulk elements include plasticity, the choice of the cohesive zone parameters is not straightforward. One challenge involves deciding what portion of the fracture energy should be associated with the plastic dissipation in the bulk elements near the crack tip and what portion should be associated with the cohesive zone. Secondly, if σ_c is chosen too large then the material will exhibit infinite toughness (Yueguang and Hutchinson 1998). If the specimen does not have any existing cracks then σ_c becomes the crack-nucleation parameter and can lead to a situation where material failure is crack-nucleation controlled.

In the simulations presented in this paper, a constant fracture toughness was assigned to all interfaces in each simulation. Simulations were performed with cohesive interface fracture toughness ranging between 0 and 15 MPa$\sqrt{m}$. As a reference, experimental measurements of fracture toughness in coarse-grain polycrystalline tungsten typically range from 8–19 MPa$\sqrt{m}$ (Gumbsch 2003). The values of σ_c and δ_c were chosen so that l_z in Eq. (14) was 25 μm, which is longer than the shortest interface element length. A coefficient of friction of 0.2 was applied to all fracture interfaces, with the frictional force only becoming active once the interface had fractured. Nodes at the trisection of potential crack paths were disconnected creating material flaws of one element in length. This was motivated by two factors. First, it helped disconnect σ_c from the stress at which cracks nucleated. Second, it relieved the multibody contact/interface algorithm of interacting with multiple sharp corners bound at a point.

Finally, to better connect the simulations with experiment, a series of simple single crack simulations were performed at a strain rate of 10^3 s^{-1} to relate the cohesive zone toughness to the actual

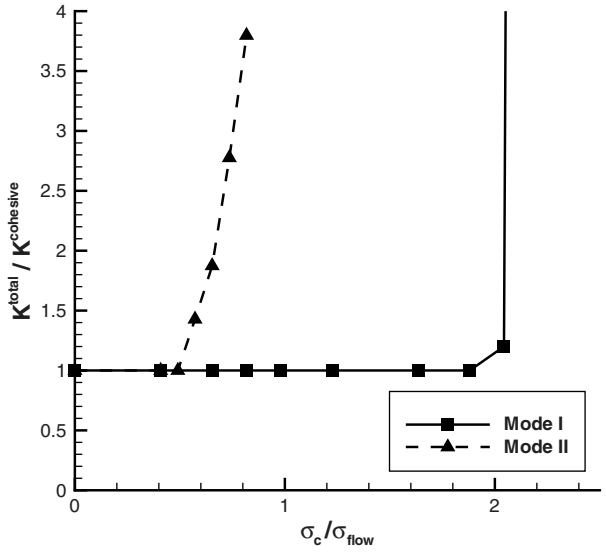

Fig. 2. Comparison of actual (total) fracture toughness with cohesive zone toughness as a function of the peak stress in the cohesive law over the uniaxial bulk plasticity flow stress; both mode I and mode II were examined with the cohesive zone length being held constant (25 μm)

mode I and mode II toughnesses that include bulk element plasticity near the crack-tip (Fig. 2). For mode I, the actual toughness measured matched that of the cohesive elements for all toughnesses less than 23 MPa$\sqrt{m}$, which for $l_z = 25$ μm corresponds to $\sigma_c = 4{,}324$ MPa, a value slightly less than twice the uniaxial flow stress (2.3 GPa). For mode II, the actual toughness followed the cohesive toughness for all toughnesses less than 6 MPa$\sqrt{m}$, which corresponds to $\sigma_c = 1{,}128$ MPa, a value slightly less than half the uniaxial flow stress. Thus, with the bulk material parameters used in this work, when the cohesive element toughnesses are higher than 6 MPa$\sqrt{m}$, the actual mode II toughness is significantly greater than the mode I toughness.

Meshing and Boundary Conditions

The primary model investigated in this work consists of approximately 600 potential fracture paths/segments generated by Voronoi tessellation of randomly positioned seeds (Fig. 3). Although the use of a Voronoi tessellation to generate a set of potential fracture paths

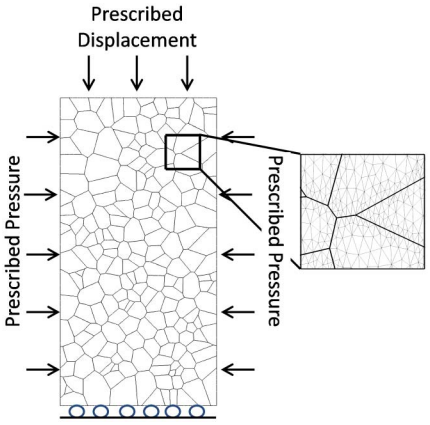

Fig. 3. Microstructure showing potential fracture paths and mesh; vertical loading (y-direction) was displacement driven, whereas confinement pressure was applied horizontally (x-direction) as a uniform constant pressure

J. Eng. Mech., 2011, 137(10): 691-698

creates a model that resembles a microstructure with weak grain boundaries, such as polycrystalline tungsten (Briant and Banerji 1983; Lassner and Schubert 1998), this analysis is not specific to a microstructure in that the bulk response is isotropic and the interpretation of the potential fracture paths is not necessarily limited to grain boundaries. The specimen was meshed with 19,190 elements with the element size refined 50% along the potential fracture paths to balance resolution and computational expense. Both the number of elements and the number of potential fracture paths were chosen as large as possible given the current computational resources and the serial nature of the contact algorithm. The simulation at the lowest strain rates required up to one month CPU time on 3-GHz xenon processors.

A uniaxial deformation was applied to the plane strain specimen by incrementing the y-displacement of the nodes along the top of the specimen while the nodes along the bottom were placed on rollers constraining their y-displacement (Fig. 3). In cases where confinement was applied, it was applied as a uniform constant pressure along the sides.

The elastic-plastic bulk constitutive law and the cohesive interfacial law set the length scale for the model. As noted in the previous section, one requirement for a mesh-independent solution is that the mesh size must resolve the cohesive zone, i.e., distance in front of a loaded crack tip where $0 < \delta_{\text{eff}} < \delta_c$ [Eq. (14)]. A second length scale that accompanies the cohesive zone model involves the interaction of multiple cracks. In the case of two cracks, when the distance between them becomes small, the cohesive zone lengths in front of each crack tip can alter their interaction. Although a physical argument could be given to justify this length-scale effect in terms of the interaction of crack-tip plastic zones, calibration to experiment would be difficult. In this work, the specimen was chosen as 3.1×6.2 mm with an average potential crack path segment of 0.2 mm. Thus, the choice of a cohesive zone length (0.025 mm in this work) should be significantly smaller than the potential crack path segment lengths while being large enough to be resolved by the mesh (quadratic elements with 0.013-mm element edge lengths along potential fracture segments).

The softening behavior of the bulk constitutive law gives rise to an additional length scale associated with strain localization [Eq. (11)]. As deformation ensues at a faster rate in regions of elevated stress, the local temperature increase softens the material and thus further increases the local deformation rate. In general, the localization of the deformation is resisted by thermal conduction (Wright 2002; Grady 1994), strain-rate hardening (Needleman 1988), and any nonlocal or strain gradient hardening in the plastic response (Fleck and Hutchinson 2001). As a result of the strain-rate hardening feature of the plasticity model used in this work, plastic localization will occur over a finite region. In general, the mesh should be fine enough to resolve this region. However, because the simulations conducted in this work are solely concerned with understanding the onset of shear localization, the requirement is somewhat relaxed, as the simulations can be terminated at the onset of a dominate localized region that has not yet localized to a band of single elements.

Multi-Crack Simulation Results

The stress-strain curves for simulations with varying cohesive element fracture toughness are shown in Fig. 4 (for an applied compressive strain rate of 10^3 s^{-1}. When the cohesive element fracture toughnesses of a simulation were less than 8 MPa$\sqrt{m}$, deformation occurred in a brittle manner via axial splitting (Fig. 5). With a toughness of 8 MPa$\sqrt{m}$, shear localization and axial splitting

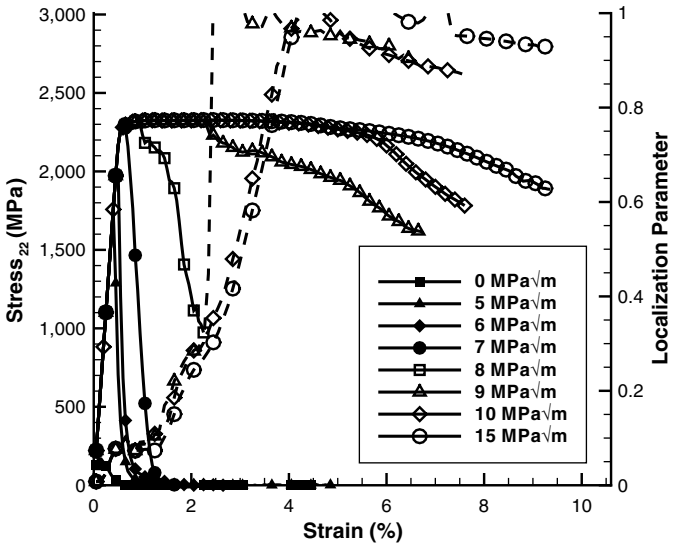

Fig. 4. Compressive stress-strain curves for simulations with varying cohesive element fracture toughnesses deformed at a constant uniaxial strain rate of 10^3 s^{-1}; the localization parameter (defined in the text and given by the dashed lines) corresponds to the degree to which deformation is localized; the localization parameter is not shown for specimens that deformed in a brittle manner

seemed to be in competition. In this case, the localization was triggered by the ejection of a few fragments from the surface. With a toughness of 9 MPa$\sqrt{m}$, failure was attributable to shear localization that resulted from a crack forming at the specimen edge near peak load. This edge crack enabled a fragment to be ejected from the specimen and induces shear localization. The simulation with a toughness of 10 MPa$\sqrt{m}$ showed no fracture at interface elements, yet shear localization occurred at lower macroscopic strains compared with the simulation with a cohesive toughness of 15 MPa$\sqrt{m}$. It is likely that this difference originates from a longer cohesive zone extending from crack path intersection defects (unconnected nodes). The subcritical displacement associated with the cohesive zone transfers more load into the bulk material and thus promotes shear localization. Although in these simulations, this effect is purely an artifact of the cohesive zone model, one could imagine an analogous scenario in a real material, where small nongrowing microcracks create a softened region that would aid in the initiation of shear localization.

To quantitatively compare the tendency for different specimens to shear localize, a shear localization parameter has been defined. In a homogeneously deforming specimen loaded in uniaxial compression, material points left of center move left, whereas points right of center move right. In a shear localizing specimen, this is not the case. In a 2D square sample where deformation is completely localized on a plane 45° off of the loading axis, one-fourth of the material points will not follow the preceding rule. For other shapes, the fraction of material points breaking the preceding rule can be easily calculated. Thus, a localization parameter can be defined where 0 represents a purely homogeneous deformation and 1 corresponds to deformation with complete shear localization on a 45° plane. Visual inspection of the specimen shows that when the localization parameter is greater than $\sim 1/3$, one would typically consider the deformation to be in the early stages of localization such that extensive localization or shear banding is imminent.

Simulations were also conducted at a strain rate of 10^4 s^{-1}. Although inertial effects are negligible for the specimen size considered in this work at an applied strain rate of 10^3 s^{-1}, at a

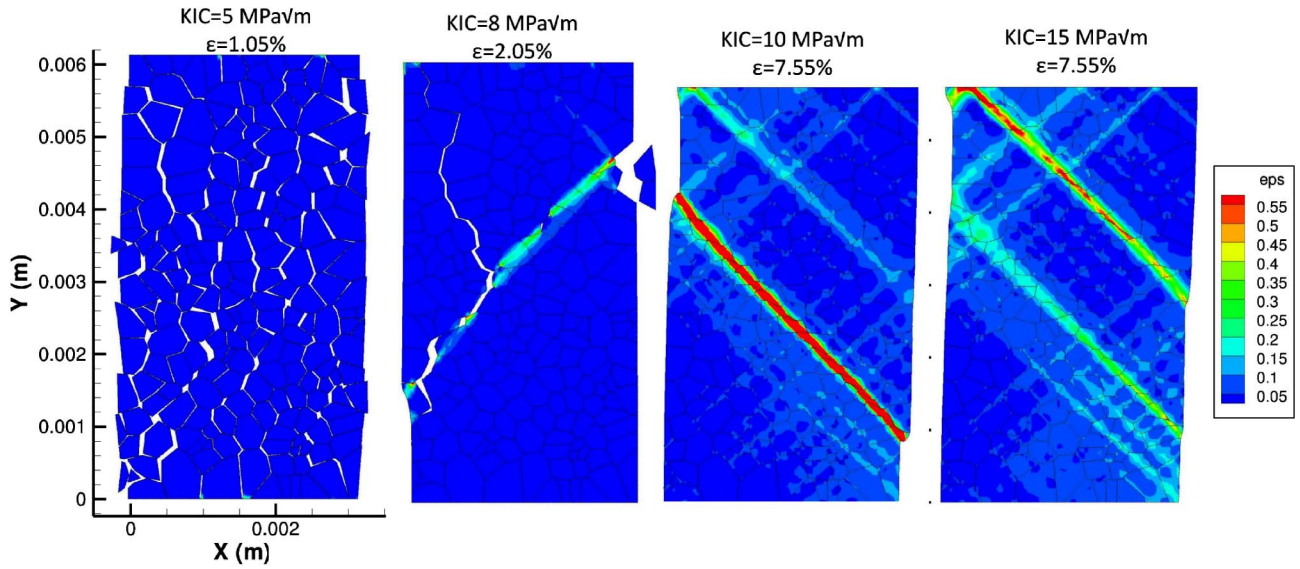

Fig. 5. Images of equivalent plastic strain in specimens with different fracture toughnesses (note the transition from brittle axial splitting to shear localization with increasing fracture toughness)

rate of 10^4 s^{-1} inertial effects are apparent and correspond to the oscillations in the postyielding portion of the stress-strain response (Fig. 6). The simulations that failed in a brittle manner at 1×10^3 s^{-1} also failed in a brittle manner at 10^4 s^{-1}, with the only difference being a prolonged softening in the stress-strain curve attributable to inertial effects. The 10^4 s^{-1} simulation with a cohesive fracture toughness of 9 MPa$\sqrt{m}$ failed in a similar fashion as the 10^3 s^{-1}, with microcrack occurring at the surface causing a fragment to be ejected, leading to shear localization. As with the 10^3 s^{-1} simulation, at 10^4 s^{-1}, the simulations with fracture toughnesses of 10 MPa$\sqrt{m}$ and 15 MPa$\sqrt{m}$ displayed no microcracking. However, the specimen with a 15 MPa$\sqrt{m}$ toughness deformed homogeneously up to a 10% strain, at which point the simulation was stopped. Thus, one may conclude that with the increase in strain rate investigated in this paper, shear localization appears to be inhibited, whereas the transition from brittle to ductile deformation remains relatively unaffected.

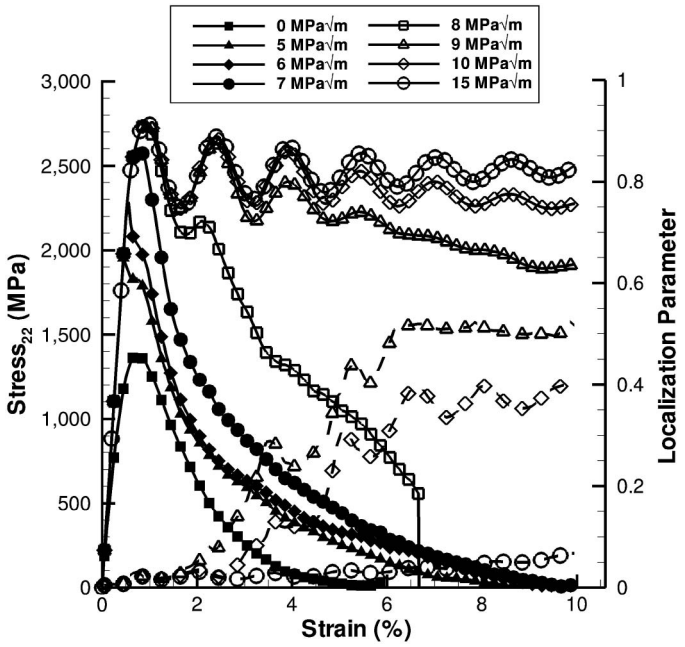

Fig. 6. Compressive stress-strain curves for simulations with various cohesive element fracture toughnesses deformed at a constant uniaxial strain rate of 10^4 s^{-1}; the localization parameter (defined in the text and given by the dashed lines) corresponds to the degree to which deformation is localized; the localization parameter is not shown for specimens which deformed in a brittle manner

The inhibition of shear localization with increasing strain rate is a trend pointed out previously by Wright (2002). In a real material, increasing the strain rate lowers the amount of heat that can be conducted away from the area of high deformation and thus allows for a local increase in temperature, leading to local material softening. At very high strain rates, where the material can be considered adiabatic, further increases in strain rate will only increase material inertia, which inhibits the onset of shear localization, as it requires a shift in momentum. Because the simulations conducted in this paper are assumed ideally adiabatic, an increased strain rate will only act to increase the inertial resistance acting against a transition from homogeneous to localized deformation.

To be relevant to KE penetrator applications, a series of simulations were conducted with a confining pressure of 1.0 GPa at a strain rate of 10^4 s^{-1} (Fig. 7). The confining pressure was applied in the x-dimension with the z-dimension being plane strain. Consistent with the brittle failure literature (Warner and Molinari 2006; Huang and Subhash 2003; Horii and Nemat-Nasser 1986; Wei and Anand 2008), confining pressure suppressed axial splitting even at the lowest fracture toughnesses. Thus the increasing tendency toward shear localization with decreasing fracture toughness continues down to zero toughness as axial splitting is suppressed. For the 10 MPa$\sqrt{m}$ simulation, shear localization is significantly less with confinement. The authors attributed this to the friction coefficient of 0.2 present at the potential crack path junction defects, which are thought to control the response of the 10 MPa$\sqrt{m}$ simulation. Confinement pressure increases the resistance to shear of these junctions, which decreases the amount of load transferred to the bulk elements prolonging the onset of shear localization.

The stress-strain responses of the confined specimens fall within three groups: zero, 5–8 MPa$\sqrt{m}$, and greater than 8 MPa$\sqrt{m}$ cohesive toughness. Micromechanically, the cracks that form in the

J. Eng. Mech., 2011, 137(10): 691-698

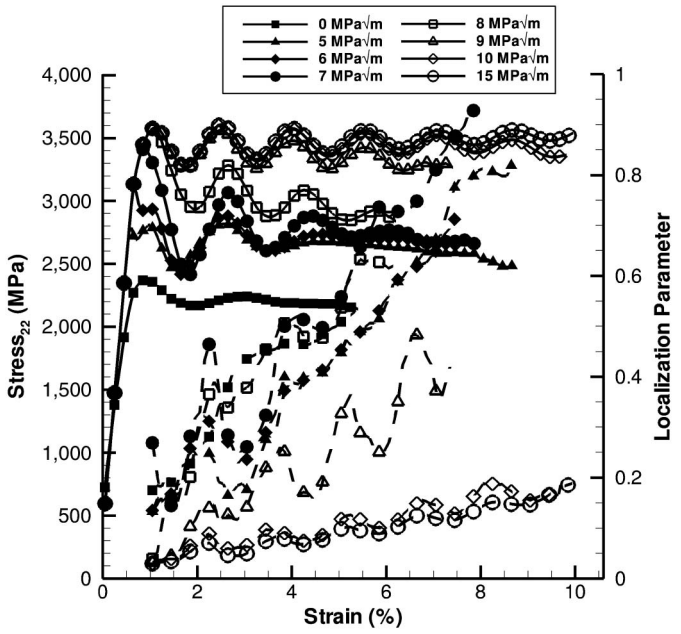

Fig. 7. Compressive stress-strain curves for simulations with various cohesive element fracture toughnesses deformed at a constant uniaxial strain rate of 10^4 s^{-1} and subjected to a uniform confining pressure of 1 GPa; the localization parameter (defined in the text and given by the dashed lines) corresponds to the degree to which deformation is localized

group with toughness values greater than 8 MPa$\sqrt{m}$ do not form a connecting network across the specimen, whereas in the intermediate regime, 5–8 MPa$\sqrt{m}$, complete fracture networks are formed. The zero toughness simulation exhibits more volumetric dilation compared with the simulations with cohesive toughnesses between 5 and 8 MPa$\sqrt{m}$.

Discussion and Bicrack Simulations

From the evolution of the stress-strain curves and the localization parameter in Figs. 4 and 6, one could conclude that, in the absence of a confining pressure, the existence of weak potential fracture paths promotes shear localization, so long as the paths are not so weak that they induce brittle failure. In the simulations key to this conclusion, i.e., those that do not fail brittlely but shear localize, two mechanisms are observed. One is the growth of a surface crack leading to the ejection of a surface fragment with shear localization ensuing from that point [Fig. 5(b)]. The second involves the noncritical cohesive zone strains transferring load to the bulk and thus promoting shear localization. While the first mechanism involving surface effects is obviously physically viable, the second may be as well, considering that the noncritical cohesive zone strains could be interpreted as microdefects or microdamage near these defects in a real material.

In the set of simulations without confining pressure, the formation of shear cracks in the interior of the material always led to mode I cracks parallel to the loading axis (wing cracks) (Horii and Nemat-Nasser 1986). Thus, one is left to inquire under what conditions or material properties would shear cracks or defects promote localizing plasticity as opposed to axial splitting. Horii and Nemat-Nasser investigated this question for a single wing crack with a discrete dislocation analytic approach (Horii and Nemat-Nasser 1986). In the absence of confining pressure, they arrived at a criterion of $0.26 = K_{IC}/\tau_y\sqrt{c\pi}$ for the transition from plasticity to axial splitting, with c being one-half of the shear crack length and τ_y being the shear flow stress. Their analysis was carried out with a coefficient of friction twice the value used in this study (0.4) and a shear crack fracture toughness of zero. Taking $\tau_y = 1.2$ GPa and $c = 0.1$ mm, their model gives a value of the mode I fracture toughness above which brittle failure will not occur of $K_{IC} = 5.5$ MPa$\sqrt{m}$. In the simulations conducted in this work, a transition from brittle to ductile behavior was observed at $K_{IC} = 9$ MPa$\sqrt{m}$. However, a direct comparison of the simulations performed in the previous section with Horri and Nemat-Nasser's model is not warranted, as the brittle to ductile transition observed in the previous section is attributable to shear cracking being suppressed, as opposed to the suppression of axial cracks growing out of shear cracks.

In this paper, the concept of shear band toughness introduced by Grady (1994) is employed to ascertain the material properties that would lead to a transition in mechanisms from shear-crack-driven axial splitting to shear-crack-enhanced shear localization. The shear band toughness ($K_{sb} = \sqrt{2\mu\gamma_{sb}}$) is a function of the energy dissipated (γ_{sb}) because of shear band propagation and is analogous to the toughness of a mode II crack. By defining a shear band toughness, the competition between axial splitting and shear localization can be studied as a simple ratio of material properties, i.e., the shear band toughness and the mode I fracture toughness.

Using a simple model with a single slant crack at 45° from the loading axis and the material properties used in the previous section, the shear band toughness was found to be 60 MPa$\sqrt{m}$ at a macroscopic uniaxial compressive strain rate of 10^3 s^{-1}. Linear elastic fracture mechanics were assumed to compute this value, despite the fact that the plastic zone size is comparable with that of the specimen. (Defining the plastic zone to be the region of material with equivalent plastic strain greater than 0.2%, it is found to extend a distance of 0.87 mm from the stress concentration immediately before the onset of macroscopic softening attributable to the localization.) This approach was chosen because it implicitly captures both the influence of the material properties and their interaction with the specimen size, allowing for a more straight forward comparison to axial cracking. As a point of reference, Grady (1994) estimates the shear band toughness of coarse-grained tungsten to be 139 MPa$\sqrt{m}$ (Table 1).

Next, the mode I fracture toughness needed to suppress axial cracking was found using the limiting case geometry most favorable to axial cracking, i.e., a potential axial crack path was placed 71° off of the slant crack (Horii and Nemat-Nasser 1986) (Fig. 8). By performing a series of simulations with varying values of mode I fracture toughness, it was found that a mode I toughness of 18 MPa$\sqrt{m}$ is sufficient to completely suppress axial cracking.

Table 1. Ratio of the Mode I Fracture Toughness to the Shear Band Toughness in the Following Materials is an Indicator of Their Tendency to Shear Band

Material	K_{sb} (MPa$\sqrt{m}$)	K_{IC} (MPa$\sqrt{m}$)	K_{IC}/K_{sb}
Aluminum 2024-T351	39	30	0.77
Steel 4340	85	80	0.94
Uranium (0.75Ti)	51	40	0.78
Coarse-grain tungsten (7Ni-3Fe)	139	15	0.11
Ultrafine-grain tungsten	60	15	0.25

Note: The value of shear band toughness of ultrafine-grain tungsten was calculated in this work, whereas all other values of shear band toughness are taken from estimates of Grady (1994). The mode I fracture toughnesses correspond to typical reported values.

J. Eng. Mech., 2011, 137(10): 691-698

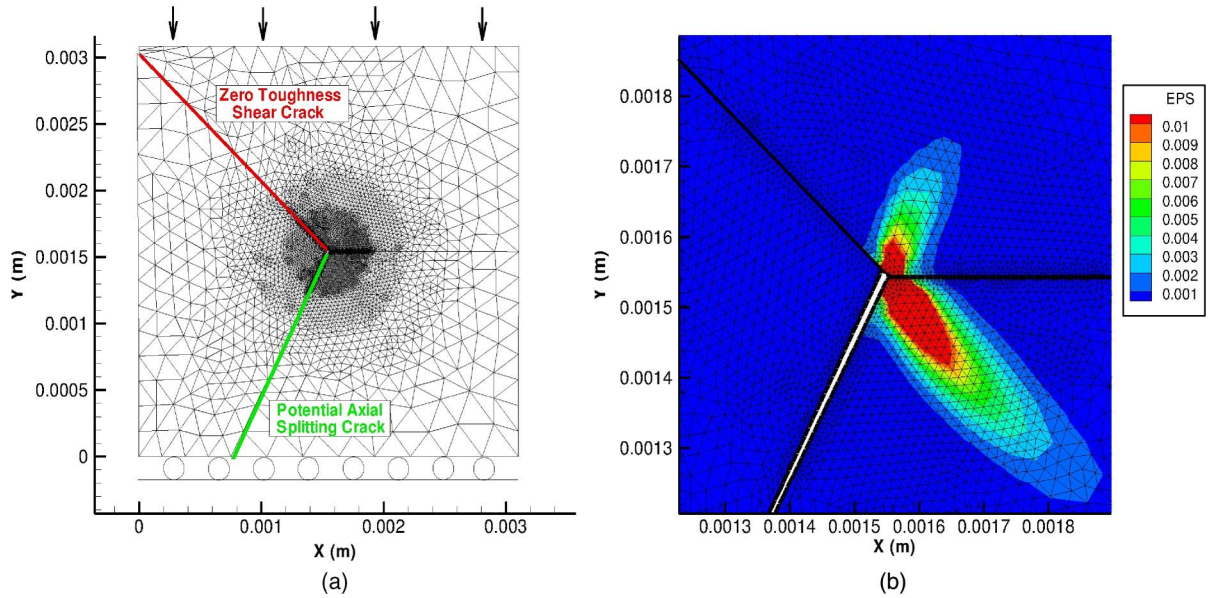

Fig. 8. (a) Model used to examine competition between shear band nucleation and axial splitting; (b) zoomed view of the tip of the shear crack at 0.5% applied macroscopic strain in a simulation with cohesive element toughnesses of 18 MPa$\sqrt{m}$ along the axial crack path; the contours represent equivalent plastic strain

This value is significantly larger than that predicted in the analytic analysis referenced previously by Horii and Nasser, 5.5 MPa$\sqrt{m}$ (Horii and Nemat-Nasser 1986). At all toughnesses less than 18 MPa$\sqrt{m}$, the simulations exhibited axial crack growth as the applied strain increased. At 0.5% applied macroscopic strain (the amount needed to nucleate a shear band in this specimen), axial crack lengths were greater than 0.9 mm for all toughnesses considered. In a multiple crack environment with crack spacing less than this value, brittle failure would be expected, consistent with the simulations in the previous section.

The limiting geometry and absence of confining pressure make 18 MPa$\sqrt{m}$ an upper limit for the fracture toughness required to inhibit axial splitting. With 1-GPa confinement and a fracture toughness of only 1 MPa$\sqrt{m}$, the axial crack is found to extend 0.1 mm at 0.5% strain. This result is consistent with the simulations performed in the previous section, as axial cracks of this length would, on average, not intersect with other cracks, and thus axial splitting would not be expected. A further consistency between the simulations performed in the previous section and the bicrack model is that an increase in strain rate from 10^3 to 10^4 s^{-1} increases K_{sb} but does not influence K_{IC} (all of the mode I fracture toughness is associated with the cohesive element dissipation at these rates), and thus, a shift away from shear localization would be expected.

To better generalize the finding that 18 MPa$\sqrt{m}$ mode I toughness is necessary to guarantee that shear cracks do not lead to brittle failure but promote shear localization, an additional series of simulations was performed with $\sigma_{y_0} = 295$ MPa, half the value of the previous simulations. Decreasing σ_{y_0} by one-half compared with the previous simulations also leads to a decrease in the flow stress by one-half. The shear band toughness of this softer material was found to be 25 MPa$\sqrt{m}$. The critical mode I toughness needed to completely suppress axial splitting was then found to be 10 MPa$\sqrt{m}$ at a strain rate of 10^3 s^{-1} with no confining pressure. This value gives $K_{IC}/K_{sb} = 40\%$ at the transition point as opposed to the 28% measured when $\sigma_{y_0} = 590$ MPa. The difference in these two ratios gives some insight into the error associated with using K_{IC}/K_{sb} (or $K_{IC}/\tau_y\sqrt{c\pi}$) to predict the transition. Despite this difference, K_{IC}/K_{sb} does appear to crudely capture the transition from brittle to shear localizing behavior over a wide range of material properties and thus may provide some guidance for materials engineering (Table 1).

Conclusions

This work has explored the influence of microcracking on a material's tendency to shear localize using a 2D finite-element framework. In the absence of a confining pressure, simulations revealed four types of behavior: brittle axial splitting, surface shear-crack-induced strain localization, cohesive-zone-induced shear localization, and homogeneous plastic flow. When an interior shear microcrack formed, it always led to the wing crack mechanism and ultimately axial splitting and brittle failure. To investigate the possibility of shear cracks promoting shear localization, as opposed to wing cracking, a simple bicrack model was employed. The geometry of the bicrack model was chosen as that most favorable to axial splitting. The preexisting shear crack produced axial splitting when the mode I fracture toughness was less than 18 MPa$\sqrt{m}$. To generalize, this value was viewed in light of the shear band toughness, and a ratio of $K_{IC}/K_{sb} = 0.28$ was found to denote the transition from axial splitting to shear localization. An additional series of simulations with half the yield stress gave a value of 0.40, confirming that K_{IC}/K_{sb} can only be considered a crude estimator of a materials proclivity toward shear localization. With a confinement pressure, both the multicrack and bicrack model exhibited shear localization with much lower fracture toughnesses. An increased strain rate hindered shear localization in both models, a finding consistent with the literature, considering the adiabatic assumption of the modeling performed in this work.

Although the 2D representation, constitutive simplifications, and cohesive element fracture methodology are all likely sources of error in the predictions of the critical K_{IC}/K_{sb} given in this work, the value of this crude metric seems to prevail beyond these assumptions when viewed in light of experimental data. With regard to the technological interest of controlling shear localization, such a metric is in line with current efforts to tailor the microstructure to reduce the strain hardening and strain-rate sensitivity of a material,

J. Eng. Mech., 2011, 137(10): 691-698

as these properties largely control K_{sb}. Other avenues for controlling strain localization, such as confinement, clearly have a strong potential so long as the confinement pressure is not so great that it reduces the shearing of existing defects in the material.

Acknowledgments

This work was supported by the Ordnance Materials Branch of the United States Army Research Laboratory under Contract No. W911 NF-07-D-0001.

References

Barenblatt, G. (1962). *The mathematical theory of equilibrium of cracks in brittle fracture. Advances in applied mechanics*, Academic Press, New York.

Bathe, K.-J., and Wilson, E. L. (1976). *Numerical methods in finite element analysis*, Prentice-Hall, Englewood Cliffs, NJ.

Belytschko, T., Liu, W. K., and Moran, B. (2000). *Nonlinear finite elements for continua and structures*, Wiley, West Sussex, UK.

Briant, C. L., and Banerji, S. K. (1983). *Embrittlement of engineering alloys*, Academic Press, New York.

Considere, A. (1885). *Ann. Des Ponts et Chaussees*, Vol. 9 (in French).

Cuitino, A., and Ortiz, M. (1992). "Material-independent method for extending stress update algorithms from small-strain plasticity to finite plasticity with multiplicative kinematics." *Eng. Comput.*, 9(4), 437–451.

Dugdale, D. (1960). "Yielding of steel sheets containing slits." *J. Mech. Phys. Solids*, 8(2), 100–104.

Fleck, N., and Hutchinson, J. (2001). "A reformulation of strain gradient plasticity." *J. Mech. Phys. Solids*, 49(10), 2245–2271.

Grady, D. E. (1994). "Dissipation in adiabatic shear bands." *Mech. Mater.*, 17(2–3), 289–293.

Gumbsch, P. (2003). "Brittle fracture and the brittle-to-ductile transition of tungsten." *J. Nucl. Mater.*, 323(2-3), 304–312.

Horii, M., and Nemat-Nasser, S. (1986). "Brittle failure in compression: Splitting, faulting and brittle-ductile transition." *Philos. Trans. R. Soc. A*, 319(1549), 337–374.

Huang, C., and Subhash, G. (2003). "Influence of lateral confinement on dynamic damage evolution during uniaxial compressive response of brittle solids." *J. Mech. Phys. Solids*, 51(6), 1089–1105.

Hughes, J. (1987). *The finite element method*, Dover, Mineola, NY.

Jonas, J. J., Holt, R. A., and Coleman, C. E. (1976). "Plastic stability in tension and compression." *Acta Metall.*, 24(10), 911–918.

Lassner, E., and Schubert, W.-D. (1998). *Tungsten—Properties, chemistry, technology of the element, alloys and chemical compounds*, Kluwer Academic/Plenum Publishers, New York.

Lennon, A. M., and Ramesh, K. T. (2000). "The thermoviscoplastic response of polycrystalline tungsten in compression." *Mater. Sci. Eng. A*, A276(1–2), 9–21.

Magness, L. S. J. (1994). "High strain rate deformation behaviors of kinetic energy penetrator materials during ballistic impact." *Mech. Mater.*, 17(2–3), 147–54.

Needleman, A. (1988). "Material rate dependence and mesh sensitivity in localization problems." *Comput. Methods Appl. Mech. Eng.*, 67(1), 69–85.

Palmer, A. C., and Rice, J. R. (1973). "The growth of slip surfaces in the progressive failure of overconsolidated clay." *Proc. R. Soc. London, Ser. A*, 332(1591), 527–548.

Stephens, J. R. (1963). "Effect of oxygen on mechanical properties of tungsten." *Tech. Rep. ADA397250 NASA-D-1581*, National Technical Information Service (NTIS), U.S. Department of Commerce, Alexandria, VA.

Taylor, L., and Flanagan, D. (1987). "Pronto2d: A two-dimensional transient solid dynamics program." *Tech. Rep. SAND86-0594*, Sandia National Laboratories, Albuquerque, NM.

Warner, D. H., and Molinari, J. F. (2006). "Micromechanical finite element modeling of compressive fracture in confined alumina ceramic." *Acta Mater.*, 54(19), 5135–5145.

Wei, Q., et al. (2006a). "Microstructure and mechanical properties of superstrong nanocrystalline tungsten processed by high-pressure torsion." *Acta Mater.*, 54(15), 4079–4089.

Wei, Y., and Anand, L. (2008). "On micro-cracking, inelastic dilatancy, and the brittle-ductile transition in compact rocks: A micro-mechanical study." *Int. J. Solids Struct.*, 45(10), 2785–2798.

Wei, Y., Su, C., and Anand, L. (2006b). "A computational study of the mechanical behavior of nanocrystalline fcc metals." *Acta Mater.*, 54(12), 3177–3190.

Wright, T. W. (2002). *The physics and mathematics of adiabatic shear bands*, Cambridge University Press, Cambridge, UK.

Yueguang, W., and Hutchinson, J. W. (1998). "Interface strength, work of adhesion and plasticity in the peel test." *Int. J. Fract.*, 93(1988), 315–333.